13026–13038 *Nucleic Acids Research, 2014, Vol. 42, No. 21* *Published online 05 November 2014*
doi: 10.1093/nar/gku1021

RNA-dependent chromatin localization of KDM4D lysine demethylase promotes H3K9me3 demethylation

Muhammad Zoabi†, Prathamesh T. Nadar-Ponniah†, Hanan Khoury-Haddad, Marko Usaj, Inbal Budowski-Tal, Tali Haran, Arnon Henn, Yael Mandel-Gutfreund and Nabieh Ayoub*

Department of Biology, Technion - Israel Institute of Technology, Haifa 3200003, Israel

Received July 20, 2014; Revised September 26, 2014; Accepted October 09, 2014

ABSTRACT

The JmjC-containing lysine demethylase, KDM4D, demethylates di-and tri-methylation of histone H3 on lysine 9 (H3K9me3). How KDM4D is recruited to chromatin and recognizes its histone substrates remains unknown. Here, we show that KDM4D binds RNA independently of its demethylase activity. We mapped two non-canonical RNA binding domains: the first is within the N-terminal spanning amino acids 115 to 236, and the second is within the C-terminal spanning amino acids 348 to 523 of KDM4D. We also demonstrate that RNA interactions with KDM4D N-terminal region are critical for its association with chromatin and subsequently for demethylating H3K9me3 in cells. This study implicates, for the first time, RNA molecules in regulating the levels of H3K9 methylation by affecting KDM4D association with chromatin.

INTRODUCTION

Histones are subjected to a variety of reversible post-translational modifications including lysine methylation, which acts as a platform for chromatin modifier proteins and leads to either gene activation or repression. Tri-methylation of histone H3 lysine 9 (H3K9me3) is enriched in condensed pericentric heterochromatin, while di-methylation (H3K9me2) and mono-methylation (H3K9me1) are associated with transcriptionally silent regions within euchromatin (1–3). Aberrant histone methylation has been linked to different human diseases including cancer (4–6).

Lysine methylation can be erased by the activity of the Jumonji C (JmjC)-domain-containing proteins that demethylate lysine through an amine oxidative reaction in the presence of iron and α-Ketoglutarate (7–10). One of the lysine demethylases (KDM) is KDM4D that specifically catalyzes the demethylation of H3K9me2/me3 (10–13). KDM4D encodes 523 amino acids containing one JmjN and one JmjC domain at its N-terminal region (encompassing amino acids 1–350), whereas the C-terminal region (encompassing amino acids 350–523) is unstructured (Figure 1A). Recent studies from our and other laboratories show that KDM4D accumulates at DNA damage sites and promotes double-strand break repair (14,15). Furthermore, various types of human cancer show misregulated expression of KDM4D (16–18). Moreover, KDM4D can also stimulate cell proliferation, survival and differentiation (19,20). How KDM4D is recruited to chromatin and recognizes its genomic binding sites is largely unknown. In this study we show, for the first time, that KDM4D binds RNA through two distinct RNA-binding domains at its N- and C-terminal regions. We also map the residues at KDM4D N-terminal region that regulate KDM4D–RNA interactions. Interestingly, we demonstrate that the binding of KDM4D to RNA is independent of its demethylase activity and reveal that the JmjC domain possesses two distinct functions: the first demethylates H3K9me3 and the second binds RNA.

Finally, we show that RNA interactions with the N-terminal domain are essential for KDM4D association with chromatin and for demethylating KDM4D histone substrate, H3K9me3, in cells.

MATERIALS AND METHODS

Plasmids constructions

The pet28a-KDM4D-6xHis, pet28a-KDM4D$^{(1–350aa)}$, pGEX-4T3-KDM4D$^{(348–523aa)}$ and pEGFP-N1-KDM4D-WT were constructed as previously described (14). The construction of the plasmids used in this study is described in Supplementary Table S1. A complete list of all the primers and their sequences is described in Supplementary Table S2. All point mutations were introduced using site-directed mutagenesis. All constructs used in this study were verified by nucleotide sequencing or restriction digestion.

Cell lines and transfection

U2OS cells and U2OS-TetON-EGFP-KDM4D cell lines were cultured as previously described (14). Transient transfections were carried out using Poly Jet (Bio Consult) or

*To whom correspondence should be addressed. Tel: +972 4 8294232; Fax: +972 4 8225153; Email: ayoubn@technion.ac.il
†The authors wish it to be known that, in their opinion, the first two authors should be regarded as Joint First Authors.

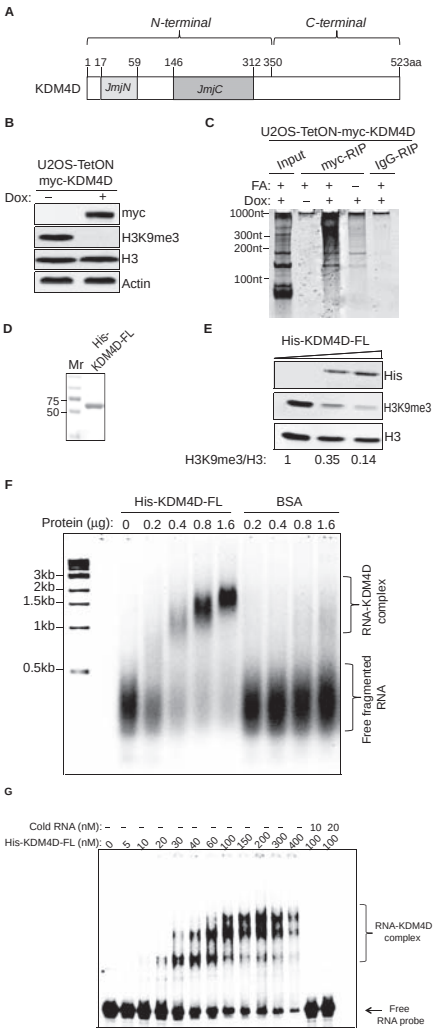

Figure 1. KDM4D histone demethylase binds RNA. **(A)** Schematic diagram of KDM4D lysine demethylase depicting the position of the N- and the C-terminal, the JmjC and the JmjN domains. aa: indicates amino acids. **(B)** Western blot showing doxycycline-dependent expression of functional myc-KDM4D fusion. Protein lysates were prepared from untreated and doxycycline-treated U2OS-TetON-myc-KDM4D and immunoblotted with the indicated antibodies. **(C)** RIP shows that myc-KDM4D protein is associated with RNA molecules in cells. U2OS-TetON-myc-KDM4D cells were subjected to RIP in the presence and absence of formaldehyde crosslinking and in untreated and doxycycline-treated cells. Results show that RNAs are associated with myc-KDM4D but not in the anti-IgG control sample. 2% of the supernatant was used as input control. **(D)** Expression and purification of full length KDM4D protein fused to 6xHis tag (His-KDM4D-FL) from bacteria. Eluted proteins were resolved by SDS-PAGE and stained with Coomassie. Mr: indicates protein marker. **(E)***In vitro* demethylation assay showing that His-KDM4D-FL demethylates H3K9me3 in a dose-dependent manner. Increasing amounts of His-KDM4D-FL were incubated with 5 μg of bulk histones. Reaction mixtures were immunoblotted using the indicated antibodies. The bands intensities of H3K9me3 were normalized relative to the intensities of their respective H3 bands and the ratios are shown at the bottom of the blot. **(F)** EMSA assay shows that KDM4D binds total RNA in a dose-dependent manner. 2.5 ug of total RNA were heat fragmented for 9 min at 90°C, incubated with His-KDM4D in EMSA binding buffer for 30 min, run in agarose gel and stained with ethidium bromide. BSA was used as a control. **(G)** EMSA shows that KDM4D binds radioactive 100nt RNA in a dose-dependent manner with estimated apparent $K_D \approx 20$ nM. As in (F), except using radioactive RNA and the reaction mixture was run in 6% native polyacrylamide gel and autoradiographed using phosphoimager. Full competition was achieved using 10 and 20 nM cold RNA as evident in the last two lanes.

TransIT®-2020 (Mirus) transfection reagents according to the manufacturer's instructions. To establish U2OS-TetON stable cell line that conditionally expresses myc-KDM4D or EGFP-KDM4D-1H4R-HRK-FL fragments including the myc-KDM4D or EGFP-KDM4D-1H4R-HRK-FL were subcloned into pTRE2-puro plasmid (Clontech). The resulting pTRE2-puro-myc-KDM4D and pTRE2-puro-EGFP-KDM4D-1H4R-HRK-FL vectors were transfected into U2OS-Tet-ON cells (Clontech). Puromycin-resistant clones (0.6 μg/ml Puromycin) were selected and tested for doxycycline-induced expression of myc-KDM4D or EGFP-KDM4D-1H4R-HRK-FL by western blot. Clones that showed expression only after the addition of 1 μM doxycycline (Sigma, D9891) were selected for further characterizations.

Western blotting and immunofluorescence

Western blotting and immunofluorescence were performed as described previously (14). A complete list of antibodies and their dilutions used in this study is described in Supplementary Table S3.

RNA-binding protein immunoprecipitation (RIP)

U2OS-TetON-myc-KDM4D cells were treated with doxycycline for 24h, and subjected to *in vivo* RNA immunoprecipitation as previously described (21) using anti-myc antibody. The RNAs that are bound to the immunoprecipitated KDM4D were extracted from the samples using Trizol reagent according to the manufacturer's protocol (Invitrogen), run in 10% denaturing urea gel and visualized by SYBR Gold.

RNase A and RNase H treatment

U2OS cells were trypsinized, washed twice with PBSX1, permeabilized with 0.05% Tween-20 in PBSX1 for 10 min on ice, washed once, resuspended with PBSX1 and treated with 1 mg/ml RNase A (Sigma) or 5U/μl of RNase H (NEB) for 30 min at RT. Cells were centrifuged at 1200 rpm and lysed in NP-40 lysis buffer (50 mM Hepes-KOH, pH 7.4, 100 mM NaCl, 0.5% NP-40, 10 mM EDTA, 20 mM β-Glycerophosphate and 1% protease inhibitor cocktail) for 10 min on ice. The cytoplasmic and nuclear fractions were isolated by centrifugation at 13 000 rpm for 5 min at 4°C. Chromatin-bound fraction was isolated by adding hot-lysis buffer as previously described (14). The biochemical fractionation shown in Figure 6A was performed as previously described (22).

Expression and purification of recombinant proteins

BL21(DE3) *Escherichia coli* cells were transformed with pet28a expression vectors, induced by IPTG (0.1 mM) for 24 hr at 18°C. Cells were lysed by EmulsiFlex (Avestin) in lysis buffer (50 mM Tris-HCl, pH 8.0, 10% glycerol, 400 mM NaCl, 5 mM β-mercaptoethanol, 15 mM Imidazole, PMSF, and protease inhibitors) treated with 25 units of Benzonase (Novagen) for 1 hr at 4°C and centrifuged for 50 min at 13 000 rpm. The recombinant proteins were then purified from

the supernatant using Ni^{+2}–NTA resin (Thermo scientific) according to manufacturer's instructions.

In vitro histone demethylation assay

Performed as described in (14,23). Briefly, 5 μg of calf thymus histones (Sigma; H9250) were incubated with 2–4 μg of purified His-tagged KDM4D protein in a demethylation buffer (20 mM Tris-HCl, pH 7.3, 150 mM NaCl, 1 mM α-ketoglutarate, 50 μM $FeSO_4$, 2 mM ascorbic acid) at 37°C for overnight. Reaction mixtures were resolved in gel and analysed by western blotting using H3K9me3 and H3 specific antibodies.

Total RNA isolation and binding assay

RNA was isolated from 293T cells using Trizol reagent (Invitrogen) according to manufacturer's instructions. Cytoplasmic and nuclear RNA from 293T cells were isolated as previously described (24). 2.5 μg of total RNA was heat fragmented for 9 min at 90°C. The binding assay was performed as previously described (25). In brief, increasing amounts of recombinant His-KDM4D-FL was incubated with the fragmented RNA in RNA binding buffer (20 mM Tris-HCl, pH 7.6, 1.5 mM $MgCl_2$, 80 mM KCl, 0.5 mM EGTA, 10% glycerol) for 30 min at RT. Samples were run in 2% Agarose gel for 60 min, 95 voltage and stained with SYBR Gold.

RNA radiolabeling

RNA oligonucleotides (1 μg) were end-labeled with [γ-^{32}P] ATP (Institute of Isotopes) using T4 polynucleotide kinase (NEB). Reactions were incubated for 1 hr at 37°C, unincorporated radioactivity were removed by G-25 spin columns (GE Healthcare) according to the manufacturer's instructions followed by purification from 10% Urea-polyacrylamide gels.

EMSAs and K_D determination

Binding reactions were carried out in 30 μl volumes of binding buffer (20 mM Tris, pH 7.4, 5 mM $MgCl_2$, 0.5 mM EGTA, 250 mM KCl, 10% (v/v) glycerol and 0.5 mg/ml BSA). Increasing concentrations of the His-KDM4D proteins were incubated with 1 μl of 2000 cpm/μl (2 nM) of ^{32}P-labeled single-stranded RNA (ssRNA). In the competitive assay, fixed amount of the protein were incubated with labeled ssRNA at RT for 20 min, then 5 or 10 folds amounts of unlabeled ssRNA were added to the reaction for 10 min. All reactions were assembled on ice and incubated at RT for 25 min. ^{32}P-labeled and unlabeled ssRNA were denatured at 70°C for 8 min and cooled on ice for 2 min before being added to the reactions. Samples were separated on 6% native polyacrylamide gels (1×Tris/Glycine buffer; 4°C; ∼1 hr at 550V). Gels were dried and exposed to phosphoimager screens. Quantification was done using Totallab quant software. K_D determination was done as described in (26). Briefly, the sums of the free and migrated RNA were defined as total RNA in the reactions. The region of the lane above RNA in RNA only reaction was defined as background and subtracted from all other lanes. The ratio between free RNA to total RNA and the migrated RNA to total RNA was calculated for each lane and the percentage complex formation was plotted as a function of KDM4D concentration using nonlinear regression analysis performed with OriginLab software.

Fluorescence anisotropy measurements and K_D determination

Equilibrium binding determined by Fluorescence Anisotropy (FA) measurements was performed with PC1 spectrofluorimeter (ISS, Champaign, Illinois) designed as T-format for simultaneous acquisition on two emission channel monochromators equipped with automatic polarizers. Fluorescein labeled RNA (IDT, Coralville, Iowa) was equilibrated with the specific protein constructs samples (60 min, room temperature). Samples were excited at λ_{ex} = 494 nm using vertical polarized light and the emitted vertical and horizontal polarized light was simultaneous monitored at λ_{em} = 523 nm. G-factor for correction of the different gain between the dual PMT detectors was calculated as described by the instrument manufacturer. The fluorescence intensity (S) and total anisotropy (A) are given by:

$$S = (GI_{||} + 2I_{\perp}) \quad (1)$$

$$A = \frac{(GI_{||} - I_{\perp})}{GI_{||} + 2I_{\perp}} \quad (2)$$

where G is the G-factor for correction of the difference gain between the parallel and perpendicular PMTs. Our binding model for a simple bimolecular reaction is as follows:

$$P + RPR; \quad K_D = \frac{[P][R]}{[PR]},$$

under the condition of $R_{tot} << K_D$ the general solution for this equilibrium binding scheme is in the form of the following quadratic equation:

$$[PR] = \frac{(P_{tot} + R_{tot} + K_D) - \sqrt{(P_{tot} + R_{tot} + K_D)^2 - 4P_{tot}R_{tot}}}{2}$$

where R_{tot} is monitoring species, P_{tot} is titrating species and *[RP]* is the bound species.

We used OriginPro software (OriginLab Corporation, Northampton, MA; Ver. 9.0) to perform NLLS fitting for the binding data.

FRAP

U2OS cell lines transfected with pEGFP-N1-KDM4D-WT or pEGFP-N1-KDM4D-1H4R-HRK were subjected to FRAP (27) with small modifications. FRAP was performed in a Zeiss LSM700 (Carl Zeiss, Germany) using a 40X oil EC Plan Neofluar objective, a zoom factor of 4 with the confocal pinhole set to 70 μm. The image size was 80×80 μm. Images were acquired every 0.458 s for GFP-KDM4D using 5% 488nm lase. The circle bleach region had a diameter of 1 μm. The bleach iteration number was set to 50 and 100% of the 488nm laser. Background was measured within

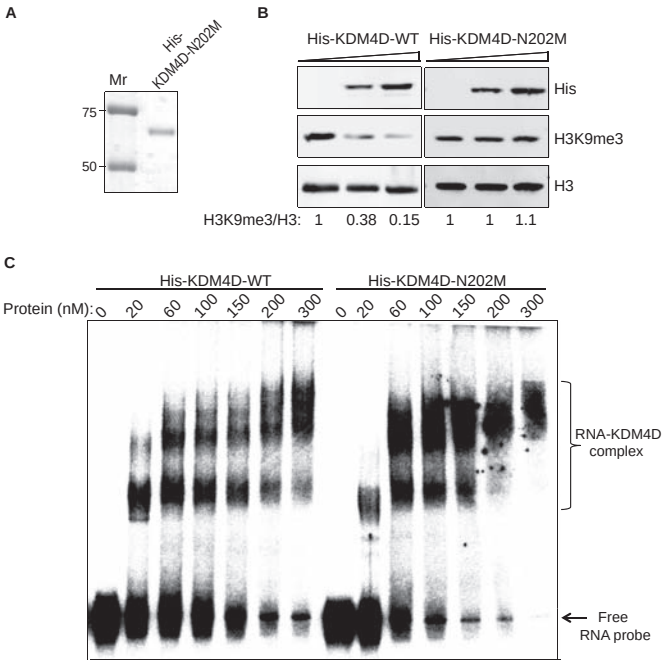

Figure 2. KDM4D binding to RNA is independent of its demethylase activity. **(A)** Coomassie staining showing the protein amount of the demethylase-dead mutant, KDM4D-N202M. Mr: indicates protein marker. **(B)***In vitro* demethylation assay showing that KDM4D-N202M is catalytically inactive. The bands intensities of H3K9me3 were normalized relative to the intensities of their respective H3 bands and the ratios are shown at the bottom of the blot. (**C**) EMSA shows similar RNA binding affinity of the wild-type (K_D≈20 nM) and the demethylase-dead mutant (K_D≈15 nM).

a region with no bleaching and subtracted from the FRAP data. The results of 12 cells were averaged and graphs were visualized in OriginLab with nonlinear regression analysis.

FLIP

In FLIP experiment (28), the cells were bleached in a rectangular region 3.5×3.5 μm. Bleaching was started after 1 scan, and the bleach iteration number was set to 30 for 160 cycles and 100% 488nm laser. Images were acquired from a rectangular region 5×5 μm after each bleaching cycle for 484 ms using 5% 488nm laser. Each bleach cycle consisted of a bleaching event of ∼1 s. To evaluate the data, the mean intensity of a rectangular region 5×5 μm was determined over time. Afterward, the background was subtracted from these results. The measurements of 12 cells were averaged in Excel, and graphs were visualized in OriginLab with nonlinear regression analysis.

Predicting the candidate RNA binding residues in KDM4D

To search for candidate RNA binding residues, an efficient structure based computational method for detecting structural similarities, named FragBag (29), was employed to compare the KDM4D structure (PDB ID: 3DXT, chain A) to all 188 226 protein chains in the PDB. The advantage of FragBag over other structural comparison methods is that it allows the detection similar sub-structures within the large data set of all possible structures. Results with a FragBag score of less than 0.3 (a threshold that assures similar structures), which were annotated in PDB as RNA binding or were part of a protein-RNA complex were considered. Further a pairwise structural alignment software was used to examine each structure, aligning it to the KDM4D sequence.

RESULTS AND DISCUSSION

KDM4D lysine demethylase is an RNA-binding protein

To study the RNA-binding of KDM4D we used RNA-binding protein immunoprecipitation (RIP) method. To this end, we established a U2OS-TetON cell line that expresses functional KDM4D-6xmyc fusion following the addition of doxycycline (Figure 1B). Untreated and doxycycline-treated cells were crosslinked using formaldehyde and subjected to RIP using myc antibody. RNA molecules that are bound to the immunoprecipitated KDM4D were purified, resolved and visualized by SYBR Gold staining. Results show that KDM4D-6xmyc is associated with RNA *in vivo* (Figure 1C). Since RIP assay can also detect indirect RNA interactions with proteins, we set up an electrophoretic mobility shift assay (EMSA) to assess direct KDM4D–RNA interactions. To do so, we have bacterially expressed and purified full-length human KDM4D protein fused to 6xHis tag (His-KDM4D-FL) (Figure1D). To assure the functionality of the His-KDM4D-FL fusion, an *in vitro* demethylation assay was carried out, where the His-KDM4D-FL protein was incubated with bulk histones and the efficiency of the demethylase activity was assessed by measuring the levels of H3K9me3 mark. Results show that His-KDM4D-FL is catalytically active and its demethylase activity increases in a dose-dependent manner (Figure 1E). To test if KDM4D can directly bind to RNA, increasing concentrations of His-KDM4D-FL protein were incubated with heat-fragmented total RNA of sizes ranging from 250 nt to 500 nt. The reaction mixtures were resolved by agarose gel electrophoresis and stained with ethidium bromide. Results show that His-KDM4D-FL protein binds total RNA in a dose-dependent manner (Figure 1F). As a control, RNA was incubated with increasing amounts of bovine serum albumin (BSA) and no significant shift in RNA mobility was observed (Figure 1F). In addition, no detectable differences were observed between the binding of heat-fragmented cytoplasmic and nuclear RNA to His-KDM4D-FL protein (Supplementary Figure S1). To determine the binding affinity of KDM4D to RNA, EMSA was performed using ^{32}P-radiolabeled random RNA sequence of 100 nt and the dissociation constant (K_D) was determined as the protein concentration at which 50% of RNA was bound (30). Results show that KDM4D binds 100 nt RNA sequence in a dose-dependent manner with apparent K_D ≈20 nM (Figure 1G). KDM4D–RNA interaction was further confirmed by competition experiments with increased amounts of unlabeled 100 nt RNA at 10 and 20 nM (last two lanes of Figure 1G). Binding curve representing the binding of His-KDM4D-FL protein to 100nt RNA is shown in Supplementary Figure S2A. To address whether His-KDM4D-FL can bind RNA sequences shorter than

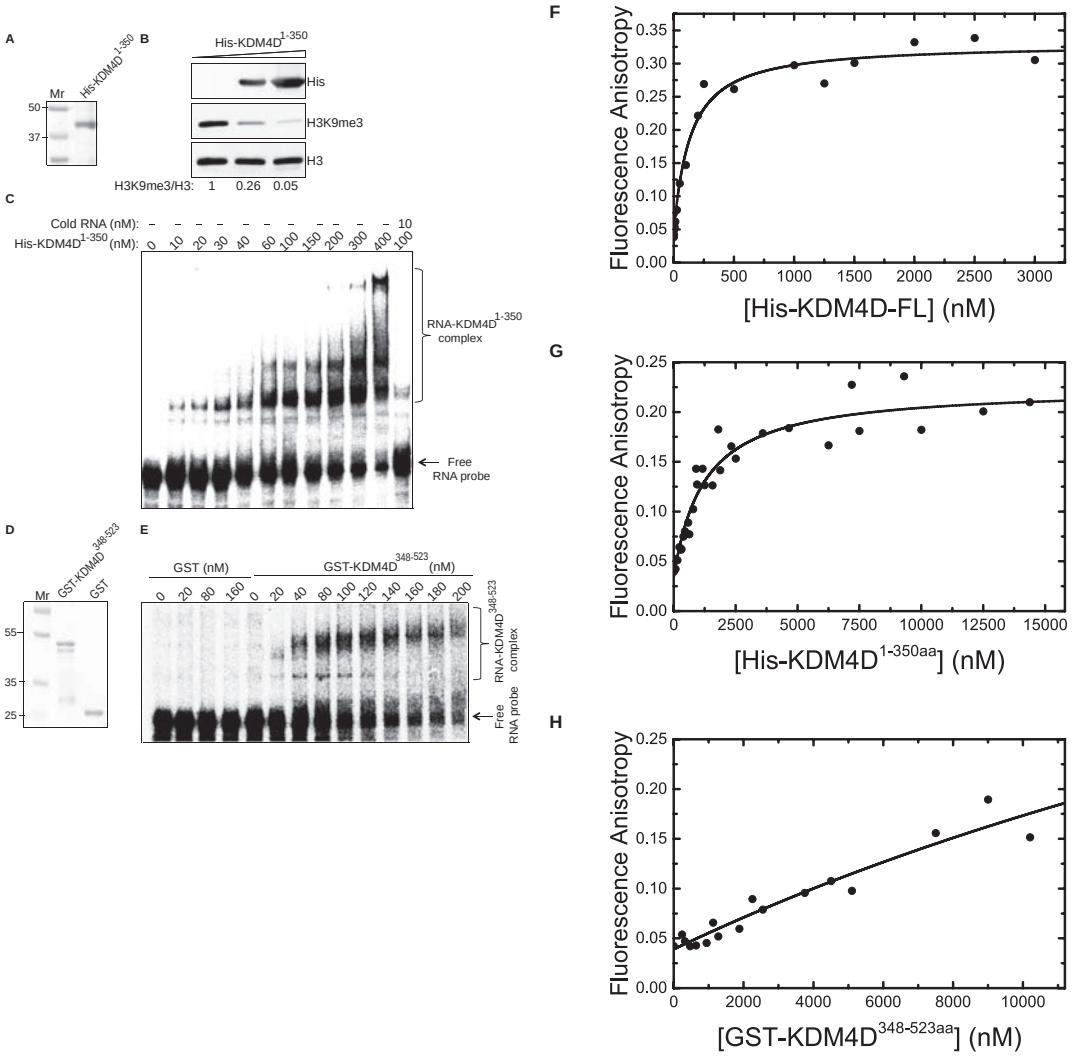

Figure 3. The N-terminal region of KDM4D (His-KDM4D$^{1–350}$) binds RNA *in vitro*. **(A)** Expression and purification of the first 350 amino acids of KDM4D protein fused to 6xHis tag (His-KDM4D$^{1–350}$). Eluted proteins were separated on SDS-PAGE gel and stained with Coomassie. Mr: indicates protein marker. **(B)** Western blot shows that His-KDM4D$^{1–350}$ is catalytically active. The i*n vitro* demethylation was performed as described in Figure 1E. The numbers below the blot indicate the relative intensities of H3K9me3 bands. **(C)** EMSA shows that His-KDM4D$^{1–350}$ binds 100nt of radioactive RNA in a dose-dependent manner with estimated apparent $K_D \approx 80$ nM. **(D)** Shows GST and GST-tagged KDM4D$^{348–523aa}$ protein stained with Coomassie. **(E)** EMSA shows that GST-KDM4D$^{348–523aa}$ binds 100 nt of radioactive RNA in a dose-dependent manner with estimated apparent $K_D > 100$ nM. GST tag was used as a negative control. (**F–H**) Equilibrium binding measurements of the [Protein]-dependence to fluorescein-labeled 22 nt RNA by fluorescence anisotropy. Data shown for the full-length (F), N-terminus (G) and C-terminus (H) of KDM4D. The best-fitted curve is shown for each graph as a black line.

100nt, we performed EMSA using 32P-radiolabeled random RNA sequence of 37 nt (correspond to the first 37 nt of the 100 nt RNA sequence). Results show that His-KDM4D-FL binds the 37nt RNA with apparent KD<50 nM, suggesting that His-KDM4D-FL's binding to RNA is length-dependent with lower affinity for shorter RNA (Supplementary Figure S3A). Binding curve obtained from EMSA results is shown in Supplementary Figure S3B. Altogether, we concluded that KDM4D is an RNA binding protein (RBP) and KDM4D–RNA interactions can occur in a sequence-independent but length-dependent manner *in vitro*.

KDM4D–RNA interaction is independent of KDM4D demethylases activity

We sought to address whether the demethylase activity of KDM4D is required for its binding to RNA. Toward this end, we generated a KDM4D demethylase-dead mutant. According to the crystal structure of KDM4D JmjC domain (12) (PDB ID: 4HON), substituting asparagine 202 with methionine is expected to disrupt the coordination of α-ketoglutarate within the catalytic site and consequently abrogates KDM4D demethylase activity. To test this prediction, we carried out an *in vitro* demethylation assay and confirmed that KDM4D-N202M is indeed a demethylase-dead protein (Figure 2A and B). Next, we used EMSA to test the ability of KDM4D-N202M mutant to bind 100 nt

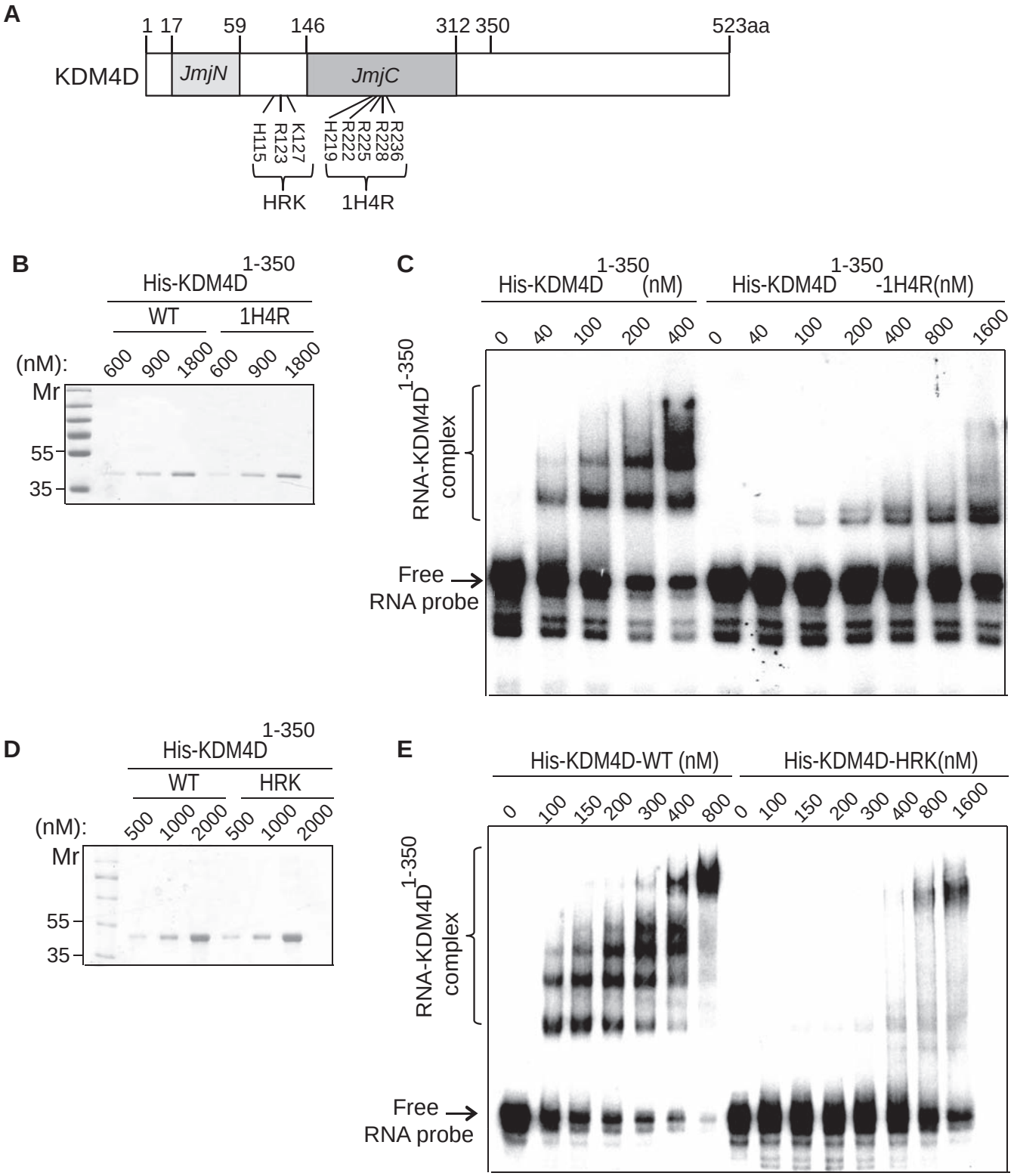
A
1 17 59 146 312 350 523aa
KDM4D
JmjN
JmjC
H115 R123 K127
H219 R222 R225 R228 R236
HRK
1H4R
B
His-KDM4D 1-350
WT 1H4R
(nM): 600 900 1800 600 900 1800
Mr
55
35
C
His-KDM4D 1-350 (nM)
His-KDM4D 1-350 -1H4R(nM)
0 40 100 200 400 0 40 100 200 400 800 1600
RNA-KDM4D 1-350 complex
Free RNA probe
D
His-KDM4D 1-350
WT HRK
(nM): 500 1000 2000 500 1000 2000
Mr
55
35
E
His-KDM4D-WT (nM)
His-KDM4D-HRK(nM)
0 100 150 200 300 400 800 0 100 150 200 300 400 800 1600
RNA-KDM4D 1-350 complex
Free RNA probe

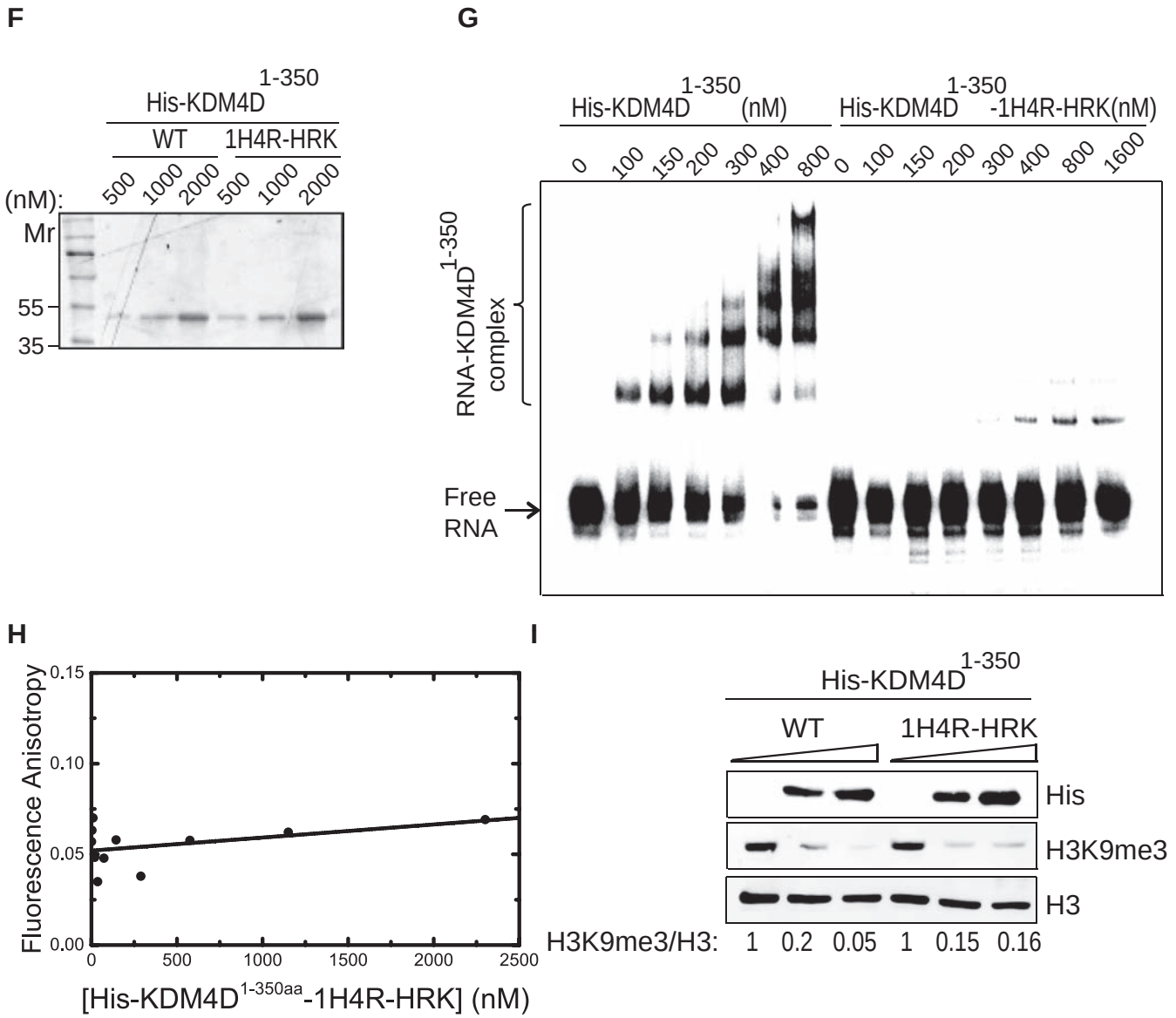

Figure 4. Establishment of KDM4D$^{1–350}$ mutant that is defective in RNA binding. **(A)** Schematic diagram of KDM4D lysine demethylase depicting the position of the amino acids that were mutated to abolish RNA binding to the N-terminal region of KDM4D. **(B)** Coomassie staining showing the purification of wild-type and His-KDM4D$^{1–350}$–1H4R mutant. **(C)** EMSA shows that KDM4D$^{1–350}$–1H4R has reduced affinity to RNA (K_D>600 nM) comparing to KDM4D$^{1–350}$-WT (K_D≈80 nM). **(D)** Coomassie staining showing the purification of wild-type and His-KDM4D$^{1–350}$-HRK mutant. **(E)** EMSA shows that KDM4D$^{1–350}$-HRK has lower binding affinity to RNA (K_D≈550 nM) comparing to wild-type (K_D>80 nM). **(F)** Coomassie staining showing the purification of wild-type and His-KDM4D$^{1–350}$–1H4R-HRK mutant. **(G)** EMSA shows that the double mutant KDM4D$^{1–350}$–1H4R-HRK lost its ability to bind RNA *in vitro*. **(H)** Equilibrium binding measurements of the [KDM4D$^{1–350}$–1H4R-HRK]-dependence to fluorescein-labeled 22 nt RNA by fluorescence anisotropy. The best-fitted curve is shown for each graph as a black line. **(I)** KDM4D$^{1–350}$–1H4R-HRK demethylates H3K9me3 *in vitro*. KDM4D$^{1–350}$ or KDM4D$^{1–350}$–1H4R-HRK was subjected to *in vitro* demethylation assay as described in Figure 1E.

RNA molecules. Results show that the RNA binding affinity of KDM4D-N202M mutant is comparable to the wild-type protein. The estimated apparent K_D of KDM4D-WT is 20 nM comparing to K_D≈15 nM for KDM4D-N202M (Figure 2C). Binding curves of KDM4D-N202M to100 nt RNA can be seen in Supplementary Figure S2B. We therefore concluded that KDM4D binding to RNA is independent of its demethylase activity.

KDM4D has two non-canonical RNA binding domains

We sought to test the ability of the KDM4D N-terminal region (encompassing amino acids 1–350 and containing the JmjN and JmjC domains) to bind RNA. Toward this end, we purified a catalytically active His-KDM4D$^{1–350}$ protein (Figure 3A and B). EMSA shows that His-KDM4D$^{1–350}$ protein binds 100 nt RNA in a dose-dependent manner with apparent K_D ≈80 nM (Figure 3C). Furthermore, competition assay using 10 nM unlabeled RNA severely impairs KDM4D$^{1–350}$-RNA interaction (Figure 3C, last

lane). Binding curves representing the binding of His-KDM4D$^{1–350}$ protein to 100 nt RNA are shown in Supplementary Figure S2C. This result suggests that the N-terminal region of KDM4D has a lower affinity to RNA ($K_D \approx$ 80 nM) comparing to the full-length KDM4D protein ($K_D \approx$ 20 nM).

The lower RNA binding affinity of KDM4D N-terminal region compared to the full-length protein suggests that KDM4D protein has an additional RNA binding region at its C-terminus. To address this point, we performed EMSA using the C-terminal region fused to GST (GST-KDM4D$^{348–523aa}$) (expressing the C-terminal of KDM4D fused to 6xHis tag proved unsuccessful (14)). Results show that GST-KDM4D$^{348–523aa}$ binds 100 nt RNA with apparent K_D>100 nM. GST was used as a control and no significant shift in RNA mobility was observed (Figure 3D and E). Binding curves obtained from the EMSA result of GST-KDM4D$^{348–523aa}$ is shown in Supplementary Figure S2D. We concluded therefore that KDM4D has two distinct RNA binding domains mapped to the N- and C-terminal regions.

To further substantiate our conclusion, we used Fluorescence Anisotropy (FA), a complementary fluorescence-based approach, to measure the equilibrium-binding constant of fluorescein labeled 22 nt RNA (RNA$^{F\text{-}22}$) to His-KDM4D-FL, His-KDM4D$^{1–350aa}$ and GST-KDM4D$^{348–523aa}$. The protein concentration-dependent binding to RNA exhibits hyperbolic behavior for His-KDM4D-FL and His-KDM4D$^{1–350aa}$, but not for the His-KDM4D$^{348–532aa}$. In agreement with the results obtained by EMSA measurements, our FA equilibrium binding determined that His-KDM4D-FL has stronger binding affinity with $K_D \approx$ 126±22 nM compared to $K_D \approx$ 1217± 246 nM for His-KDM4D$^{1–350aa}$ (Figure 3F and G, respectively), suggesting again the contribution of the KDM4D C-terminal to RNA binding. The small differences in the affinity observed by FA and EMSA could be due to either the shorter RNA substrate used in FA and/or the differences in the methodologies. We also measured the RNA binding affinity of the GST-KDM4D$^{348–532aa}$. However, it did not exhibit any hyperbolic dependence on the protein concentration up to 10 fold higher than needed for saturation by His-KDM4D-FL (Figure 3H). We assumed therefore that the affinity for the GST-KDM4D$^{348–532aa}$ is very weak and we estimated K_D> 5000 nM. Nonetheless, this region must contribute to the overall affinity as observed when comparing the His-KDM4D-FL with His-KDM4D$^{1–350}$.

Characterization of the RNA binding domain at the N-terminus of KDM4D

We sought to map the residues within the N-terminal of KDM4D that regulate its interaction with RNA. Given that KDM4D does not possess any canonical RNA binding domain, we used BindN software (31) to predict residues that might interact with RNA. This analysis revealed two close stretches of 8 amino acids (87–94 and 106–113) between the JmjN and the JmjC domains that have high confidence score for binding RNA (Supplementary Figure S4A). Therefore, we generated KDM4D-16M mutant, where the 16 residues were substituted with alanine, and proceeded to testing its RNA binding ability by EMSA. Results show that KDM4D-16M mutant has only slightly weaker RNA binding affinity ($K_D \approx$ 28 nM) than KDM4D wild-type ($K_D \approx$ 20 nM), suggesting that the mutated residues are not implicated in KDM4D–RNA interactions (Supplementary Figure S4B). The binding curve of KDM4D-16M mutant is shown in Supplementary Figure S4C. This result prompted us to look for RNA binding motifs within the catalytic JmjC domain. We searched for arginine-rich motifs within the JmjC domain as these motifs are found in several known RBP and provide a platform for binding RNA (32). We observed that the sixth and the seventh alpha helixes of the JmjC domain (10) contain four exposed arginine residues (arginine-222, 225, 228, 236) and one histidine residue (histidine 219) that can provide a binding site for RNA (Figure 4A and Supplementary Figure S5A). To address this prediction, His-KDM4D$^{1–350}$–1H4R mutant, which includes the substitution of the histidine and the four arginine residues with alanine, was tested for its ability to bind RNA. EMSA shows that the RNA binding affinity of His-KDM4D$^{1–350}$–1H4R mutant is significantly reduced with estimated K_D> 600 nM comparing to $K_D \approx$ 80 nM for KDM4D wild-type (Figure 4B and C). This result strongly suggests that the mutated residues of the JmjC domain provide an interface for binding RNA. To specify additional RNA binding regions within KDM4D, we searched the structural database (PDB) for homologous structures already known to bind RNA. Using Fragbag software (see materials and methods), we revealed 10 structures of candidate RNA binding proteins. Among these 10 candidates was the cleavage and polyadenylation specificity factor subunit 6 (PDB ID: 3P6Y, chain A), which showed a relatively high structural similarity to KDM4D (Supplementary Figure S5A). Interestingly, the local region, which aligned best to KDM4D, included the known RNA binding residues of the cleavage factor. Based on the homology results we selected 3 surface residues on KDM4D close to the JmjC domain, histidine-115, arginine-123 and lysine-127 (hereafter called HRK), which were aligned to specific residues on the cleavage factor known to bind RNA (Figure 4A and Supplementary Figure S5B). As above, we substituted the HRK residues with alanine to generate His-KDM4D$^{1–350}$-HRK mutant. EMSA shows that the RNA binding affinity of KDM4D$^{1–350}$-HRK is severely reduced with K_D> 550 nM. This result suggests that the HRK residues are also involved in KDM4D–RNA interactions (Figure 4D and E). Next, we sought to address whether the combination of the 1H4R and the HRK mutations has cumulative effects on KDM4D binding to RNA. To do so, we generated His-KDM4D$^{1–350}$–1H4R-HRK mutant that includes the substitution of 1H4R and HRK residues to alanine and tested its ability to bind RNA. EMSA shows that KDM4D$^{1–350}$–1H4R-HRK mutant lost its ability to bind RNA (Figure 4F and G). Binding curves for His-KDM4D$^{1–350}$–1H4R, His-KDM4D$^{1–350}$-HRK, and His-KDM4D1^{-350}–1H4R-HRK are shown in Supplementary Figure S6. Equilibrium binding experiments of His-KDM4D$^{1–350}$–1H4R-HRK mutant to RNA$^{F\text{-}22}$ (Figure 4H) by FA exhibit basically no binding up to 2500 μM in comparison to $K_D \approx$1217 ± 246 nM

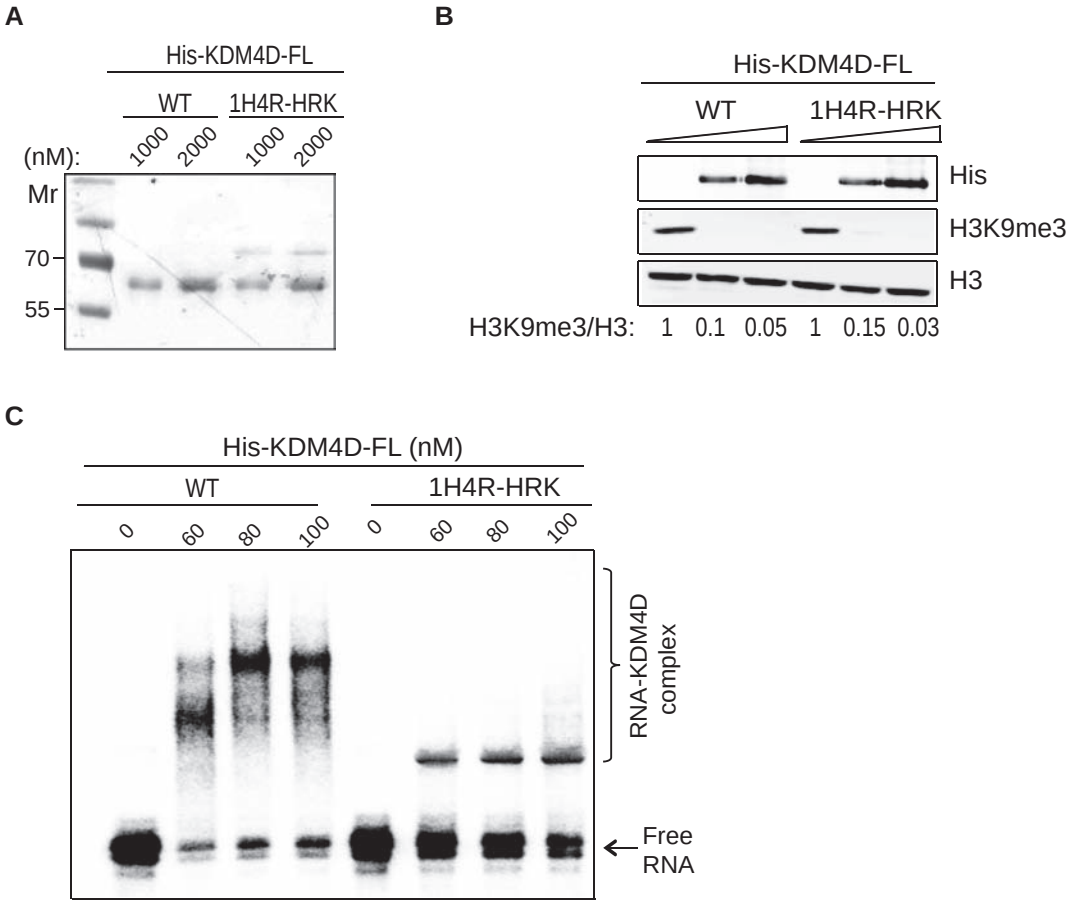

Figure 5. The full-length KDM4D-1H4R-HRK mutant is defective in RNA binding. **(A)** Coomassie staining showing the purification of wild-type His-KDM4D-FL and His-KDM4D-FL-1H4R-HRK mutant. **(B)** KDM4D-FL-1H4R-HRK demethylates H3K9me3 *in vitro*. *In vitro* demethylation assay was performed as described in Figure 1E, except of using His-KDM4D-FL-1H4R-HRK and His-KDM4D-FL as a control. **(C)** EMSA shows defective RNA binding of His-KDM4D-FL-1H4R-HRK mutant comparing to wild-type protein.

for His-KDM4D$^{1–350}$ (Figure 3G). This is again in agreement with the EMSA results. Altogether, we mapped the regions within the JmjC domain that mediate KDM4D–RNA interactions. Next, we sought to address whether the demethylase activity of KDM4D$^{1–350}$–1H4R-HRK mutant, which is defective in RNA binding, was affected. *In vitro* demethylation assay shows that the catalytic activity of KDM4D$^{1–350}$–1H4R-HRK mutant is indistinguishable from the N-terminal His-KDM4D$^{1–350}$ protein (Figure 4I). This important finding allows us to draw two conclusions: first, that defective RNA binding of KDM4D$^{1–350}$–1H4R-HRK is not due to its incorrect folding as it retains its demethylase activity. Second, we genetically uncoupled the catalytic KDM4D demethylase activity from its ability to bind RNA *in vitro*.

Next, the 1H4R-HRK mutations were introduced into the full-length KDM4D coding sequence and the observed His-KDM4D-FL-1H4R-HRK mutant (Figure 5A) was tested for its ability demethylate histones and to bind RNA. Results show that whereas the *in vitro* demethylase activity of His-KDM4D-FL-1H4R-HRK mutant remains intact (Figure 5B), its interactions with RNA were disrupted and show different RNA binding pattern comparing to the wild-type His-KDM4D-FL protein (Figure 5C). The Binding curve shows that His-KDM4D-FL-1H4R-HRK has K_D > 100 nM (Supplementary Figure S7). The ability of His-KDM4D-FL-1H4R-HRK to bind RNA is likely mediated by the second RNA binding domain at its C-terminal region.

RNA interaction with KDM4D N-terminus is essential for KDM4D association with chromatin

Given the emerging role of RNA molecules in recruiting various protein complexes to chromatin (33), we sought to test whether KDM4D interaction with RNA is required for its association with chromatin. Initially, we showed using biochemical fractionation that KDM4D is enriched at the chromatin-bound fraction (Figure 6A). Next, to address whether RNA molecules are required for the chromatin localization of KDM4D, U2OS cells were mock or RNase A treated and subjected to biochemical fractionation using NP-40 lysis buffer (see materials and methods). Results show that RNase A treatment severely disrupts the localization of KDM4D at the NP40-resistant-fraction, suggesting that RNA molecules might be indeed required for KDM4D association with chromatin (Figure 6B). Similarly, the chromatin localization of PARP1 was also disrupted

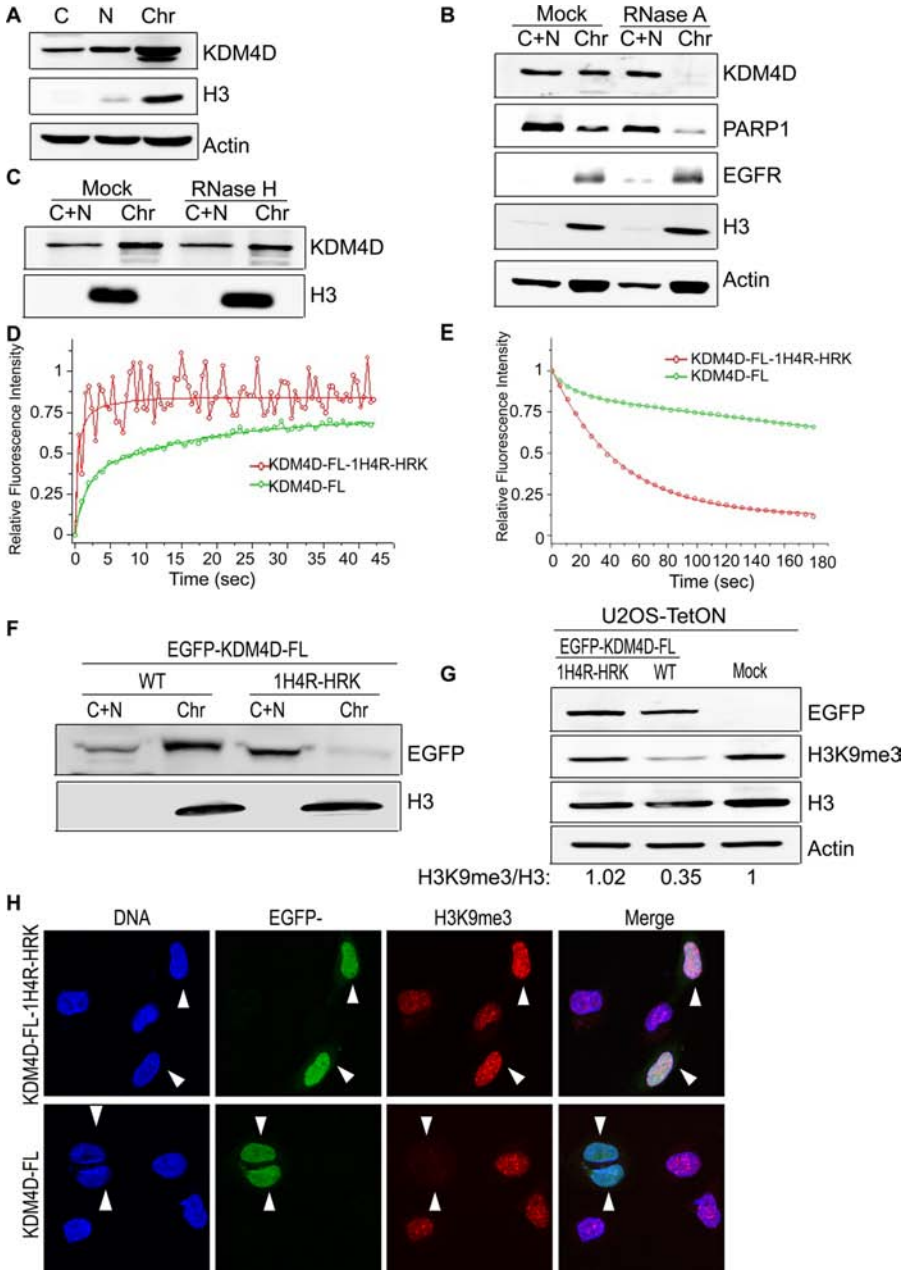

Figure 6. RNA interactions with KDM4D N-terminal region are critical for KDM4D association with chromatin and for the demethylation of H3K9me3 mark. **(A)** KDM4D is enriched at the chromatin-bound fraction. U2OS cells were subjected to biochemical fractionation as previously described (22). Samples from the different fractions were resolved and immunoblotted using the indicated antibodies. **(B)** RNase A treatment disrupts the KDM4D localization at the NP-40-resistant fraction. Mock and RNase A-treated cells were subjected to biochemical fractionation using NP-40 lysis buffer and protein samples were resolved and immunoblotted using the indicated antibodies. **(C)** The chromatin localization of KDM4D is not affected by RNase H treatment. U2OS cells were treated with Mock or RNase H and subjected to biochemical fractionation as described in (B). **(D** and **E)** FRAP and FLIP analyses show that the 1H4R-HRK mutations lead to a remarkable increase in the mobility of KDM4D in cells. U2OS cells were transfected with constructs encoding EGFP-KDM4D-WT or EGFP-KDM4D-1H4R-HRK and subjected to FRAP (D) or FLIP (E) assay. In (D) the plot shows the relative fluorescence intensity over time at the bleached area, normalized to the pre-bleached levels. In (E) the cells were subjected to continuous bleaching in a particular area and the relative fluorescence at a nearby region was plotted against time. The FRAP and the FLIP results are the averages for 12 different cells and similar results were obtained in two different experiments. **(F)** Biochemical fractionation shows that, unlike EGFP-KDM4D-WT, EGFP-KDM4D-FL-1H4R-HRK lost its association with chromatin. **(G)** Shows that overexpression of EGFP-KDM4D-FL-1H4R-HRK has no detectable effect on the overall levels of H3K9me3. U2OS-TetON cells were treated with doxycycline for 24 h to induce the expression of EGFP-KDM4D-FL or EGFP-KDM4D-FL-1H4R-HRK, and protein extracts were prepared using hot-lysis procedure and subjected for western blotting using the indicated antibodies. The intensities of H3K9me3 bands were normalized against the corresponding H3 signal and the ratios are shown at the bottom of the blot. (**H**) Representative cells showing that EGFP-KDM4D-FL-1H4R-HRK is unable to demethylate H3K9me3 mark (red). Cells were transfected with constructs encoding either EGFP-KDM4D-WT or EGFP-KDM4D-1H4R-HRK mutant (green) and subjected to immunofluorescence analysis. Nuclei were stained with DAPI (blue). These results are typical of 3 independent experiments and at least 30 different cells were acquired each time. White arrowheads indicate cell transfected with EGFP-KDM4D-WT (top) and EGFP-KDM4D-FL-1H4R-HRK mutant (bottom). C: cytoplasmic; N: nuclear soluble fraction; Chr: chromatin-bound fraction.

in RNase A-treated cells (Figure 6B). This result is consistent with previous report showing that noncoding RNA (ncRNA) molecules mediate PARP1 association with chromatin (34). On the other hand, the localization of histone H3 and EGFR1, a known chromatin-bound protein were not affected by RNase A treatment, suggesting that RNase A treatment has no global disruptive effect on the localization of chromatin proteins (Figure 6B). To get further insight on the identity of the RNA molecules that might regulate KDM4D localization to chromatin, U2OS cells were treated with RNase H, which specifically cleaves RNA-DNA duplexes. We observed that, unlike RNase A, RNase H treatment has no detectable effect on the chromatin localization of KDM4D (Figure 6C). This result suggests that RNA molecules that form a duplex with DNA are not involved in KDM4D chromatin localization.

The effect of RNase A treatment on KDM4D localization indicates that RNA molecules might be required for KDM4D association with chromatin. To further substantiate this observation, we applied interventional microscopy techniques to measure the mobility of KDM4D-FL-1H4R-HRK mutant. U2OS cells were transfected with constructs encoding either EGFP-KDM4D-FL-1H4R-HRK or EGFP-KDM4D-FL-WT and subjected to Fluorescence Recovery After Photobleaching (FRAP) assay, where we recorded the recovery of fluorescence signal in the bleached area by time-lapse imaging. FRAP shows that ∼40% of EGFP-KDM4D-FL-WT molecules are immobile with halftime of recovery $t_{1/2} = 2.5$ s (Figure 6D). This result is in line with our previous findings, showing that KDM4D is enriched at the chromatin bound fraction (Figure 6A). In contrast, EGFP-KDM4D-FL-1H4R-HRK is highly mobile as less than 10% of the molecules are immobile and show a remarkable faster recovery of the fluorescence signal with $t_{1/2} = 0.6$ s (Figure 6D). To further validate the mobilization of EGFP-KDM4D-FL-1H4R-HRK mutant, we used a complementary approach called Fluorescence Loss In Photobleaching (FLIP), which can detect more accurately the exchange of high mobility molecules. In FLIP, the cells are exposed to continuous bleaching and the rate of fluorescence loss is measured in a nearby region of the bleached area. Results show that the rate of fluorescence loss of KDM4D-FL-1H4R-HRK mutant is much faster than KDM4D-FL-WT and only 9% of the fluorescence signal of EGFP-KDM4D-FL-1H4R-HRK remains after 67 bleach pulses comparing to 43% of EGFP-KDM4D-FL-WT (Figure 6E). Collectively, these observations strongly suggest that the mobilization of the defective RNA binding KDM4D-FL-1H4R-HRK mutant results from its inability to bind chromatin. Indeed, biochemical fractionation shows a dramatic decrease in the levels of KDM4D-FL-1H4R-HRK mutant at the chromatin-bound fraction (Figure 6F). This observation further confirms the defective association of KDM4D-FL-1H4R-HRK mutant with chromatin.

Next, we wanted to address whether the inability of KDM4D-FL-1H4R-HRK mutant to bind chromatin affects its ability to demethylate histones *in vivo*. Toward this, cells expressing KDM4D-FL-WT and KDM4D-FL-1H4R-HRK mutant were subjected to western blot and immunofluorescence analysis and stained with H3K9me3 antibody. Results demonstrate that overexpression of EGFP-KDM4D-FL-1H4R-HRK mutant has no effect on H3K9me3 levels. On the other hand, cells expressing KDM4D-FL-WT protein show a dramatic decrease in H3K9me3 intensity (Figure 6G and H). These observations suggest that the RNA-dependent association of KDM4D with chromatin is critical for demethylating H3K9me3 on chromatin.

We show here, for the first time, that the JmjC-containing demethylase, KDM4D, is an RBP. We mapped the RNA binding regions and demonstrated that KDM4D N-terminal-RNA interaction is critical for its association with chromatin and for its *in vivo* H3K9me3 demethylation. Future studies will be required to decipher the biological significance of the interactions between KDM4D C-terminal region and RNA and to identify whether the RNA sequences that bind KDM4D *in vivo* are specific or non-specific. Noticeably, EMSA experiments (*e.g.* Figure 1G) show that the addition of increasing amounts of KDM4D protein results in the appearance of multiple shifted bands of KDM4D–RNA complexes, which correspond most likely to the binding of multiple KDM4D molecules to one molecule of RNA. The appearance of multiple retarded bands was reported for several known RNA binding proteins such as, hnRNP F, Fox-1 and ZNF180ZF (35), SCML2 (36) and hnRNPK (37).

Given that some of KDM4D residues that mediate its interaction with RNA are conserved across the JmjC-containing demethylases, we propose that other KDM proteins are recruited to chromatin by similar mechanisms. In this regard, it should be noted that according to the catalog of somatic mutations in cancer (http://www.sanger.ac.uk/cosmic), four of the residues that mediate KDM4D–RNA interactions, arginine-123, arginine-225, arginine-222 and lysine 127 are mutated in lung, esophagus and large intestine carcinomas. Interestingly, the aforementioned mutations might disrupt other activities of KDM4D. For example, we have recently shown that KDM4D is recruited to DNA breakage sites in a PARP1-dependent manner (14). Follow-up studies will be needed to knock in 1H4R-HRK mutations into the endogenous KDM4D gene and assess their effect on KDM4D recruitment and subsequently on double-strand breaks repair.

Our findings are in line with growing number of evidence implicating RNA molecules in regulating chromatin structure and organization (33,38,39). For examples, snoRNAs interact with Df31 decondensation factor protein to open the chromatin and promote transcription (25). Moreover, ncRNA interacts with chromatin remodeling complexes such as SWI/SNF to induce transcriptional silencing (40). Interestingly, ncRNAs play a central role in modulating histone methylation. For instance, Xist ncRNA recruits PRC2 repressive complex that promotes H3K27 methylation to silence X chromosome (41,42). The Air ncRNA promotes H3K9me3 by recruiting G9a methyltransferase to its genomic binding sites (43). Furthermore, it was shown that HOTAIR ncRNA binds PRC2, known to drive H3K27 methylation, and LSD1, capable of catalyzing H3K4 demethylation (44). Finally, by showing that the disruption of KDM4D–RNA interactions inhibits the demethylation of H3K9me3 by KDM4D, we hereby pro-

vide a novel avenue for developing small molecules inhibitor that target KDM4D catalytic activity in cancer driven by KDM4D amplification.

SUPPLEMENTARY DATA

Supplementary Data are available at NAR Online.

ACKNOWLEDGEMENT

We are grateful to Noga-Guttmann-Raviv for her help in the biochemical fractionation described in Figure 6A. To Gadi Schuster and his lab manager Varda Liveanu for their help in synthesizing and radiolabeling the RNA for EMSA experiments. We thank Nitzan Dahan from the Life Sciences and Engineering Infrastructure Unit at the Technion, for his help performing FLIP assay.
Author contributions: Muhammad Zoabi: performed the experiments described in Figures 1D, E, G, 2A, B, 3A, B, C, F, G, H, 4B, C, H, I, 6D, E, F, G, H, Supplementary Figure S2A, S2B, S2C, S2D, S3B, S4A, S4C, S5A, S6 and S7B, also did in vitro RNA transcription and radioactive labeling of all RNA used in EMSA. Prathamesh T Nadar-Ponniah: performed the experiments described in Figures 1C, F, 2C, 3D, E, 4D, E, F, G, J, 5A, B, C, 6A, B, C, Supplementary Figure S1, S3A, S4B, S7A. Hanan Khoury-Haddad established U2OS-TetON-myc-KDM4D cell line, performed the experiment described in Figure 1B and helped in FRAP and FLIP analysis. Tali Haran contributed to setting up EMSA and provided the equipment and lab space for performing the EMSA analysis. Marko Usaj and Arnon Henn designed, performed, and analysed the Fluorescence Anisotropy experiments in Figures 3F, G, H and 4H. Inbal Budowski-Tal: designed and performed the computational analyses defining the RNA binding region shown in Supplementary Figure S5B. Yael Mandel-Gutfreund helped in designing the computational analyses. Nabieh Ayoub conceived the study, planed the experiments and wrote the paper.

FUNDING

Israel Cancer Research Fund (ICRF) [2015211]; Israel Science Foundation [2014673]; the Israel Cancer association [2019404]; the H. Blechman and Eliayu Pen Memorial Cancer Research Fund [2018025]. Funding for open access charge: Israel Cancer Research Fund (ICRF); Israel Science Foundation; the Israel Cancer association; the H. Blechman and Eliayu Pen Memorial Cancer Research Fund.
Conflict of interest statement. None declared.

REFERENCES

1. Peters,A.H., O'Carroll,D., Scherthan,H., Mechtler,K., Sauer,S., Schofer,C., Weipoltshammer,K., Pagani,M., Lachner,M., Kohlmaier,A. *et al.* (2001) Loss of the Suv39h histone methyltransferases impairs mammalian heterochromatin and genome stability. *Cell*, **107**, 323–337.
2. Cheutin,T., McNairn,A.J., Jenuwein,T., Gilbert,D.M., Singh,P.B. and Misteli,T. (2003) Maintenance of stable heterochromatin domains by dynamic HP1 binding. *Science*, **299**, 721–725.
3. Schotta,G., Lachner,M., Sarma,K., Ebert,A., Sengupta,R., Reuter,G., Reinberg,D. and Jenuwein,T. (2004) A silencing pathway to induce H3-K9 and H4-K20 trimethylation at constitutive heterochromatin. *Genes Dev.*, **18**, 1251–1262.
4. Black,J.C., Van Rechem,C. and Whetstine,J.R. (2012) Histone lysine methylation dynamics: establishment, regulation, and biological impact. *Mol Cell*, **48**, 491–507.
5. Zhang,X., Wen,H. and Shi,X. (2012) Lysine methylation: beyond histones. *Acta Biochim. Biophys. Sin. (Shanghai)*, **44**, 14–27.
6. Greer,E.L. and Shi,Y. (2012) Histone methylation: a dynamic mark in health, disease and inheritance. *Nat. Rev. Genet.*, **13**, 343–357.
7. Klose,R.J., Kallin,E.M. and Zhang,Y. (2006) JmjC-domain-containing proteins and histone demethylation. *Nat. Rev. Genet.*, **7**, 715–727.
8. Tsukada,Y., Fang,J., Erdjument-Bromage,H., Warren,M.E., Borchers,C.H., Tempst,P. and Zhang,Y. (2006) Histone demethylation by a family of JmjC domain-containing proteins. *Nature*, **439**, 811–816.
9. Whetstine,J.R., Nottke,A., Lan,F., Huarte,M., Smolikov,S., Chen,Z., Spooner,E., Li,E., Zhang,G., Colaiacovo,M. *et al.* (2006) Reversal of histone lysine trimethylation by the JMJD2 family of histone demethylases. *Cell*, **125**, 467–481.
10. Chen,Z., Zang,J., Whetstine,J., Hong,X., Davrazou,F., Kutateladze,T.G., Simpson,M., Mao,Q., Pan,C.H., Dai,S. *et al.* (2006) Structural insights into histone demethylation by JMJD2 family members. *Cell*, **125**, 691–702.
11. Hillringhaus,L., Yue,W.W., Rose,N.R., Ng,S.S., Gileadi,C., Loenarz,C., Bello,S.H., Bray,J.E., Schofield,C.J. and Oppermann,U. (2012) Structural and evolutionary basis for the dual substrate selectivity of human KDM4 histone demethylase family. *J. Biol. Chem.*, **286**, 41616–41625.
12. Krishnan,S. and Trievel,R.C. (2013) Structural and functional analysis of JMJD2D reveals molecular basis for site-specific demethylation among JMJD2 demethylases. *Structure*, **21**, 98–108.
13. Shin,S. and Janknecht,R. (2007) Diversity within the JMJD2 histone demethylase family. *Biochem. Biophys. Res. Commun.*, **353**, 973–977.
14. Khoury-Haddad,H., Guttmann-Raviv,N., Ipenberg,I., Huggins,D., Jeyasekharan,A.D. and Ayoub,N. (2014) PARP1-dependent recruitment of KDM4D histone demethylase to DNA damage sites promotes double-strand break repair. *Proc. Natl Acad. Sci. U.S.A.*, **111**, E728–E737.
15. Young,L.C., McDonald,D.W. and Hendzel,M.J. (2013) Kdm4b Histone Demethylase Is a DNA Damage Response Protein and Confers a Survival Advantage following gamma-Irradiation. *J. Biol. Chem.*, **288**, 21376–21388.
16. Black,J.C., Manning,A.L., Van Rechem,C., Kim,J., Ladd,B., Cho,J., Pineda,C.M., Murphy,N., Daniels,D.L., Montagna,C. *et al.* (2013) KDM4A Lysine Demethylase Induces Site-Specific Copy Gain and Rereplication of Regions Amplified in Tumors. *Cell*, **154**, 541–555.
17. Berry,W.L. and Janknecht,R. (2013) KDM4/JMJD2 histone demethylases: epigenetic regulators in cancer cells. *Cancer Res.*, **73**, 2936–2942.
18. Labbe,R.M., Holowatyj,A. and Yang,Z.Q. (2013) Histone lysine demethylase (KDM) subfamily 4: structures, functions and therapeutic potential. *Am. J. Transl. Res.*, **6**, 1–15.
19. Kim,T.D., Oh,S., Shin,S. and Janknecht,R. (2012) Regulation of tumor suppressor p53 and HCT116 cell physiology by histone demethylase JMJD2D/KDM4D. *PLoS One*, **7**, e34618.
20. Zhu,Y., van Essen,D. and Saccani,S. (2012) Cell-type-specific control of enhancer activity by H3K9 trimethylation. *Mol. Cell*, **46**, 408–423.
21. Niranjanakumari,S., Lasda,E., Brazas,R. and Garcia-Blanco,M.A. (2002) Reversible cross-linking combined with immunoprecipitation to study RNA-protein interactions in vivo. *Methods*, **26**, 182–190.
22. Mendez,J. and Stillman,B. (2000) Chromatin association of human origin recognition complex, cdc6, and minichromosome maintenance proteins during the cell cycle: assembly of prereplication complexes in late mitosis. *Mol. Cell. Biol.*, **20**, 8602–8612.
23. Ipenberg,I., Guttmann-Raviv,N., Khoury,H.P., Kupershmit,I. and Ayoub,N. (2013) Heat shock protein 90 (Hsp90) selectively regulates the stability of KDM4B/JMJD2B histone demethylase. *J. Biol. Chem.*, **288**, 14681–14687.
24. Rio,D.C., Ares,M. Jr, Hannon,G.J. and Nilsen,T.W. (2010) Preparation of cytoplasmic and nuclear RNA from tissue culture cells. *Cold Spring Harbor protocols*, **2010**, doi:10.1101/pdb.prot5441.

25. Schubert,T., Pusch,M.C., Diermeier,S., Benes,V., Kremmer,E., Imhof,A. and Langst,G. (2012) Df31 protein and snoRNAs maintain accessible higher-order structures of chromatin. *Mol. Cell*, **48**, 434–444.
26. Di Ruscio,A., Ebralidze,A.K., Benoukraf,T., Amabile,G., Goff,L.A., Terragni,J., Figueroa,M.E., De Figueiredo Pontes,L.L., Alberich-Jorda,M., Zhang,P. *et al.* (2013) DNMT1-interacting RNAs block gene-specific DNA methylation. *Nature*, **503**, 371–376.
27. Ayoub,N., Jeyasekharan,A.D., Bernal,J.A. and Venkitaraman,A.R. (2008) HP1-beta mobilization promotes chromatin changes that initiate the DNA damage response. *Nature*, **453**, 682–686.
28. Shimi,T., Koujin,T., Segura-Totten,M., Wilson,K.L., Haraguchi,T. and Hiraoka,Y. (2004) Dynamic interaction between BAF and emerin revealed by FRAP, FLIP, and FRET analyses in living HeLa cells. *J. Struct. Biol.*, **147**, 31–41.
29. Budowski-Tal,I., Nov,Y. and Kolodny,R. (2010) FragBag, an accurate representation of protein structure, retrieves structural neighbors from the entire PDB quickly and accurately. *Proc. Natl Acad. Sci. U.S.A.*, **107**, 3481–3486.
30. Cho,S., Hoang,A., Sinha,R., Zhong,X.Y., Fu,X.D., Krainer,A.R. and Ghosh,G. (2011) Interaction between the RNA binding domains of Ser-Arg splicing factor 1 and U1–70K snRNP protein determines early spliceosome assembly. *Proc. Natl Acad. Sci. U.S.A.*, **108**, 8233–8238.
31. Wang,L. and Brown,S.J. (2006) BindN: a web-based tool for efficient prediction of DNA and RNA binding sites in amino acid sequences. *Nucleic Acids Res.*, **34**, W243–W248.
32. Burd,C.G. and Dreyfuss,G. (1994) Conserved structures and diversity of functions of RNA-binding proteins. *Science*, **265**, 615–621.
33. Batista,P.J. and Chang,H.Y. (2013) Long noncoding RNAs: cellular address codes in development and disease. *Cell*, **152**, 1298–1307.
34. Guetg,C., Scheifele,F., Rosenthal,F., Florian,F., Hottiger,M.O. and Santoro,R. (2012) Inheritance of Silent rDNA Chromatin is Mediated by PARP1 via Noncoding RNA. *Mol. Cell*, **45**, 1–11.
35. Bendak,K., Loughlin,F.E., Cheung,V., O'Connell,M.R., Crossley,M. and Mackay,J.P. (2012) A rapid method for assessing the RNA-binding potential of a protein. *Nucleic Acids Res.*, **40**, e105.
36. Bonasio,R., Lecona,E., Narendra,V., Voigt,P., Parisi,F., Kluger,Y. and Reinberg,D. (2014) Interactions with RNA direct the Polycomb group protein SCML2 to chromatin where it represses target genes. *eLife*, **3**, e02637.
37. Evans,J.R., Mitchell,S.A., Spriggs,K.A., Ostrowski,J., Bomsztyk,K., Ostarek,D. and Willis,A.E. (2003) Members of the poly (rC) binding protein family stimulate the activity of the c-myc internal ribosome entry segment in vitro and in vivo. *Oncogene*, **22**, 8012–8020.
38. Castello,A., Fischer,B., Eichelbaum,K., Horos,R., Beckmann,B.M., Strein,C., Davey,N.E., Humphreys,D.T., Preiss,T., Steinmetz,L.M. *et al.* (2012) Insights into RNA biology from an atlas of mammalian mRNA-binding proteins. *Cell*, **149**, 1393–1406.
39. Sabin,L.R., Delas,M.J. and Hannon,G.J. (2013) Dogma derailed: the many influences of RNA on the genome. *Mol. Cell*, **49**, 783–794.
40. Zhu,Y., Rowley,M.J., Bohmdorfer,G. and Wierzbicki,A.T. (2013) A SWI/SNF chromatin-remodeling complex acts in noncoding RNA-mediated transcriptional silencing. *Mol. Cell*, **49**, 298–309.
41. Jeon,Y. and Lee,J.T. (2011) YY1 tethers Xist RNA to the inactive X nucleation center. *Cell*, **146**, 119–133.
42. Tavares,L., Dimitrova,E., Oxley,D., Webster,J., Poot,R., Demmers,J., Bezstarosti,K., Taylor,S., Ura,H., Koide,H. *et al.* (2012) RYBP-PRC1 complexes mediate H2A ubiquitylation at polycomb target sites independently of PRC2 and H3K27me3. *Cell*, **148**, 664–678.
43. Nagano,T., Mitchell,J.A., Sanz,L.A., Pauler,F.M., Ferguson-Smith,A.C., Feil,R. and Fraser,P. (2008) The Air noncoding RNA epigenetically silences transcription by targeting G9a to chromatin. *Science*, **322**, 1717–1720.
44. Chu,C., Qu,K., Zhong,F.L., Artandi,S.E. and Chang,H.Y. (2011) Genomic maps of long noncoding RNA occupancy reveal principles of RNA-chromatin interactions. *Mol. Cell*, **44**, 667–678.